Distribution.

M Caldwell RAL
B Swinyard RAL
A Richards RAL
K Dohlen LAS
M Griffin QMW
P Hargrave QMW
J Brock JPL

CONTENTS.

Summary.

Beam patterns in the FTS are given for the case of a smooth-walled circular horn, at the centre wavelengths of each channel. Both the single- & multi-mode FOV responses are modelled, & this necessitates also the calculation of the horn efficiencies for each mode. The efficiency & FOV width are plotted versus wavelength in section 3.

For the longest wavelength channel (worst-case for component sizing & diffracted stray-light) , the beam patterns at key components are also given (App.C). This is for the case of beam clipping by the cold-stop only, & calculation of any additional clipping is to be included later when component size restrictions are known.
The main problem shown so far is in the FTS collimating mirrors, which have adjacent edges & so can't be oversized. At long wavelengths a stray beam is produced but it should be possible to trap this with a baffle.

1. Propagation model (reverse).

1.1 Beam patterns at components.

Fig.1 shows the FTS system propagation model. The input beam is defined at the detector (object #19), with X of the pattern chosen to lie along X of the system, and it is propagated outwards through the optics (i.e. in time-reversed sense).

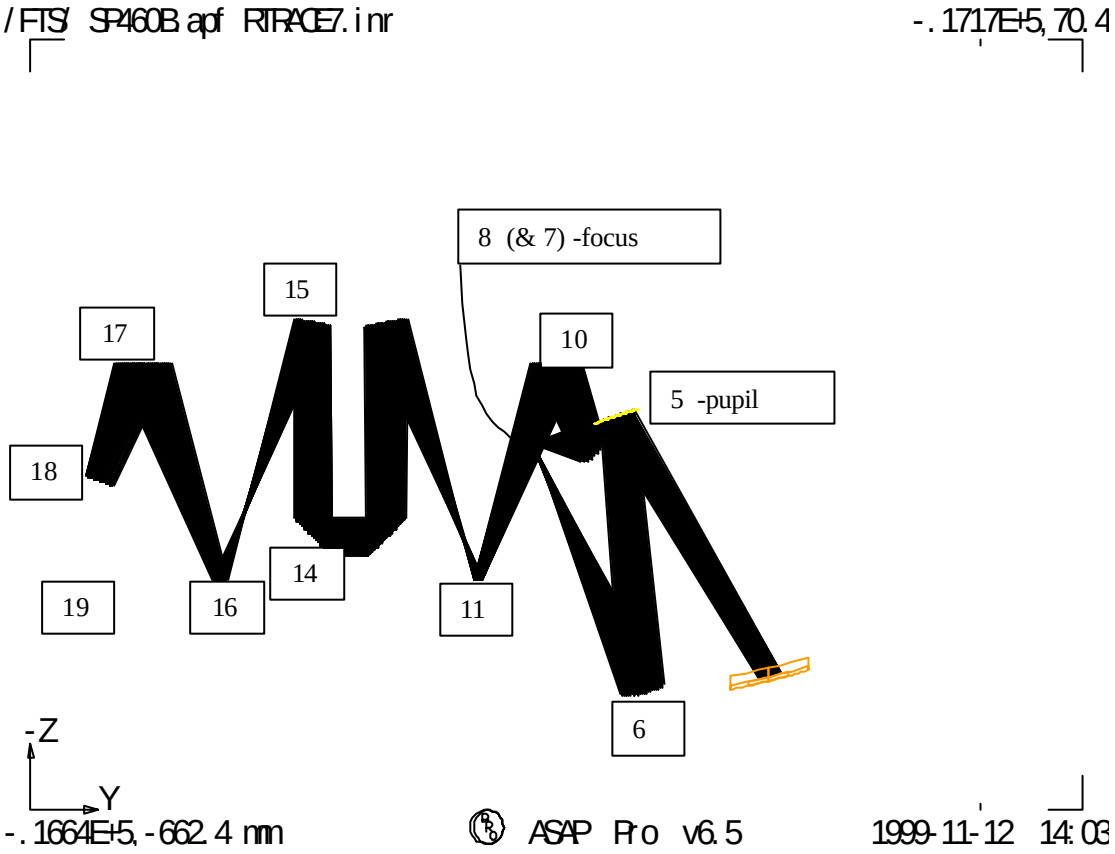

Fig.1. FTS model, design ref. sp460b.

The beam is first clipped at the cold stop (Obj 18). In the current model no further clipping is applied. Therefore initially we are looking at how the F/5 beam pattern looks at each component, in the case where all components are adequately oversized with respect to the cold stop. In addition the far-field beam patterns should be representative of those from other systems having similar detector, F-number & low aberrations, for example the on-axis case in BACUS.

Further clippings that will need to be added are those due to the field stops (wavelength & array position dependent) and the Lyot stops (wavelength dependent).

1.2 Horn aperture efficiency.

This is the purely interference effect of the field amplitude & phase mis-matches between the beam (approx. Airy pattern) and any given horn mode. The efficiency

may be calculated as a surface integral across any plane of the beam, and the calculation method is given in appendix A.

The horn aperture radius is a fixed parameter chosen as

$$a = (2.F.\lambda_{des}-t)/2 \qquad (1)$$

where t is the allowable thickness of material between apertures, taken as 0.1mm here. λ_{des} is the design wavelength.

The horn length L is a free parameter (to some extent) and at the aperture it determines the horn field's wavefront radius of curvature, but not its amplitude distribution. For ideal field matching to the Airy pattern's flat wavefront at focus, L should be large. However the accommodation constraint limits L , and the optimum coupling is then achieved by introducing some defocus as illustrated in fig.2, to give the beam field some wavefront curvature to match that of the horn field. Such a defocus also changes the beam amplitude pattern at the horn, increasing its width & so reducing the amplitude overlap between the fields. As a result there is a trade-off between the amplitude & the wavefront matching requirements, and for a given L the defocus is adjusted to optimise the net efficiency. In addition, since SPIRE is an array instrument with close-packed detectors, any such defocus could not be made large without introducing significant cross-talk between adjacent detectors.

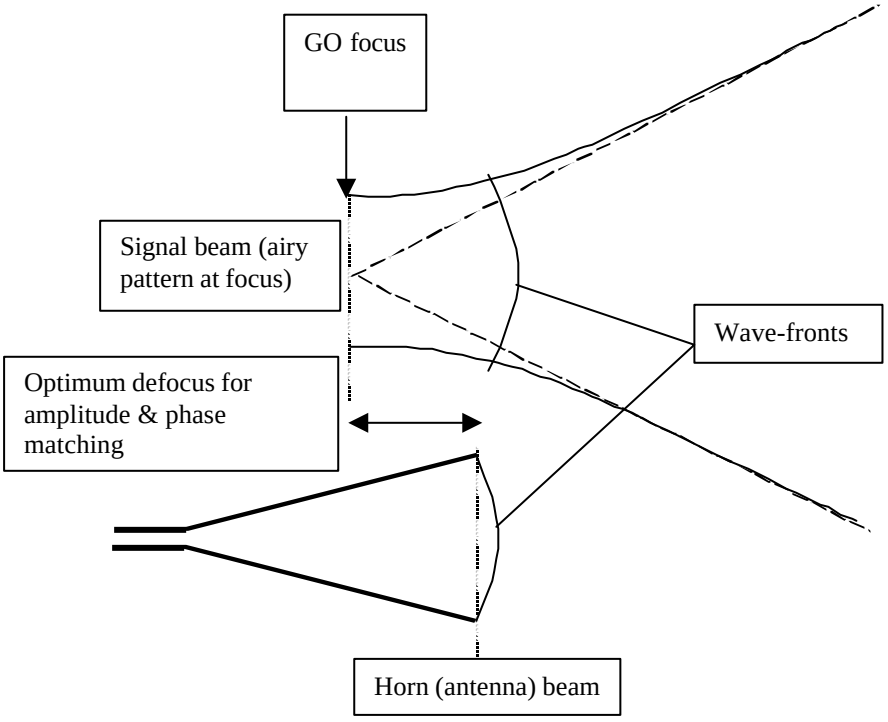

Fig.2. Geometry for calculation of horn aperture efficiency (ref.2).

In order to model this focus optimisation, it is easiest to chose the horn aperture plane for evaluation of η (appendix).

1.3 Field-of-view (PST) response.

The point source transmittance (PST) response on the sky is a spatial convolution of the horn beam pattern with that of the Airy-pattern signal beam, and for a single-moded horn (gaussian-like beam) matched to the Airy pattern size, this has a shape close to that given by the horn beam pattern propagated through the optics (the so-called antenna pattern).

Here we consider only this horn beam pattern, as representative of the PST. Its pattern on the sky can be obtained as a simple scaling of the pattern at any image plane (field stop) prior to the instrument pupil (cold stop), and for this purpose we use the antenna pattern at the pick-off mirror (object 8 in fig.1 above). The method used for propagation of the horn pattern through the optics to the pick-off mirror, is detailed in appendix C.

In the case of single-moded operation (long wavelengths) a single efficiency is involved, but for multi-mode operation, some assumptions have to be made about how each mode contributes to the net PST. The current assumption is that the responsivity of the bolometric detecting element, and the waveguide losses, are the same in all modes & at all wavelengths.

The net intensity response I_{tot} in the multi-moded case, is then calculated as the sum of the normalised intensity patterns of all M propagating modes, weighted by their horn efficiencies η_m as defined above :

$$I_{tot} = \sum_{m=0}^{M-1} I_m h_m$$

and the integral is over a plane perpendicular to the beam direction.

In this calculation the effect of clipping by the cold stop is taken into account by the η values (Although these were calculated at the plane of the horn aperture, the result is the same as obtained if the plane of the cold stop is used). Any optics effect of Lyot stop or field stop clipping on the relative mode strengths is not included in the current model.

2. Input mode patterns.

We show here the mode patterns at the horn for long wavelength first, since at long wavelength there is just 1 mode , and further modes are added progressively as we go to shorter wavelengths. The SPIRE channel centre wavelengths of 0.5, 0.35 & 0.2 mm, have respectively 2, 3 & 7 modes propagating. The patterns are given by analytic equations from ref.1.

2.1 Long wavelength (> 0.55mm).

in its lowest order mode, i.e. TE11, smooth-walled circular horn. The E-field at the horn aperture is as per fig.3.

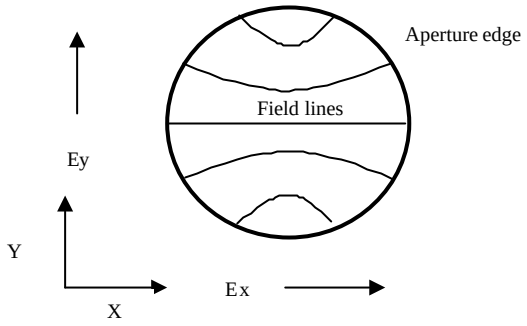

Fig.3a. E-field pattern of mode.

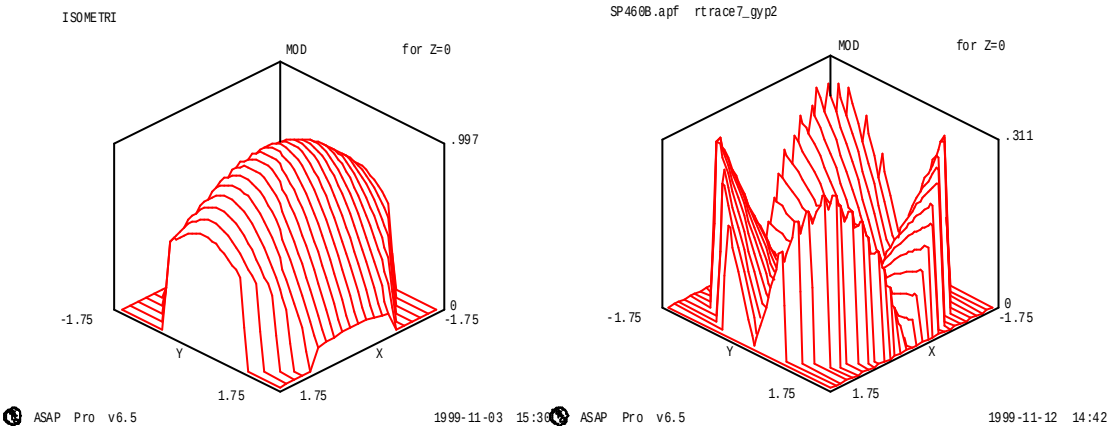

Fig.3b. Input field modulus in cartesian components: Ex (left), Ey (right).
NB. maximum Ex is larger, the peak Ey field is 30% of the peak Ex.

The actual field data is shown in fig.3b. *In all beam plots the lateral scale is in millimetres.* Here λ_{des}=0.35mm for which equation 1 gives aperture radius ~1.75mm.

A discussion of how such a mode pattern is converted to elementary beamlets for propagation in our model is given in appendix B.

Fig.4. shows a comparison of horn & signal fields for the case of this mode.

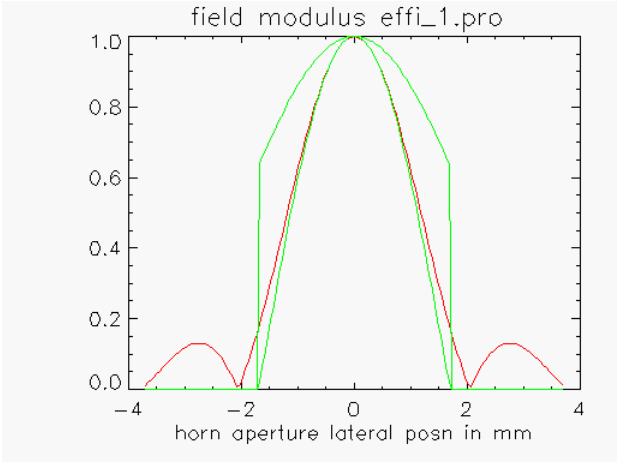

Fig.4. Signal beam field (red) and mode field (green, in 2 principal sections), for TE11 mode at $\lambda=\lambda_{des}$=350um.

2.2 Intermediate wavelength 0.35mm.

Here there are two additional modes propagating, these being the TM01 & TE21 whose patterns are shown below.

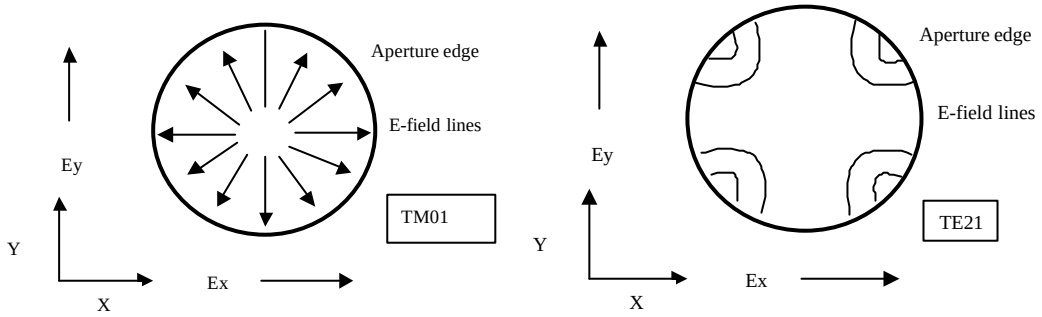

Fig.5. E-field patterns of TM01 & TE21 modes.

In the x- and y-sections plotted in fig.6. the 2 modes have identical profiles, but in 2-D they have different patterns.

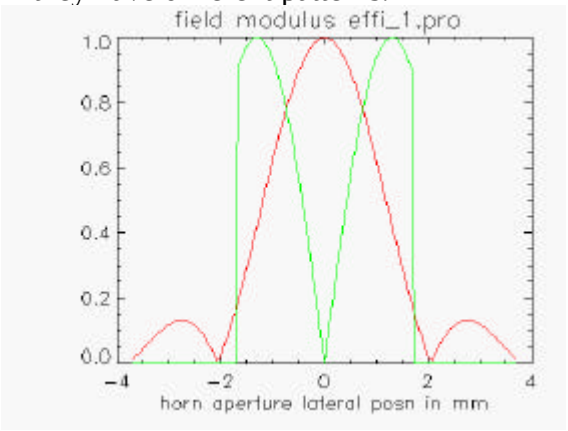

Fig.6. Signal beam (Airy pattern) & mode X- & Y- profiles, for TM01 & TE21 modes.

2.3 Short wavelength 0.2mm.

By this point there are an additional 4 modes propagating (making 7 in total). These are the TM11,TE01,TM21 & TE31 modes, whose patterns are shown below.

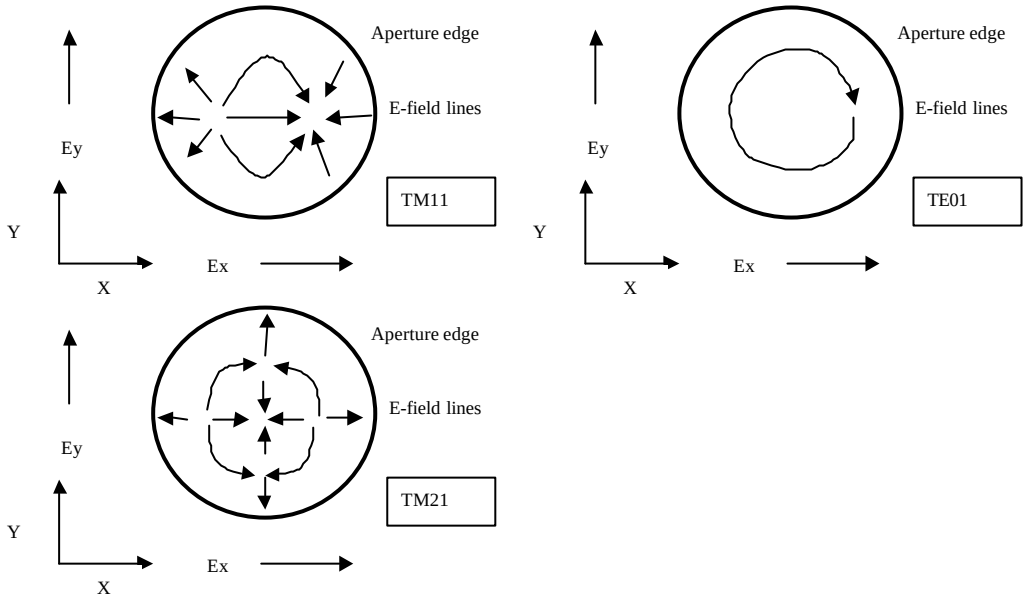

3. Results.

3.1 Detector horn efficiency.

Case of horn aperture sized for 0.35mm wavelength.

Figs. 1 & 2 show the model's results for total horn efficiency & FOV function FWHM, calculated at the wavelengths 0.35, 0.5 & 0.67 mm, at which there are respectively 3, 2 & 1 modes propagating.

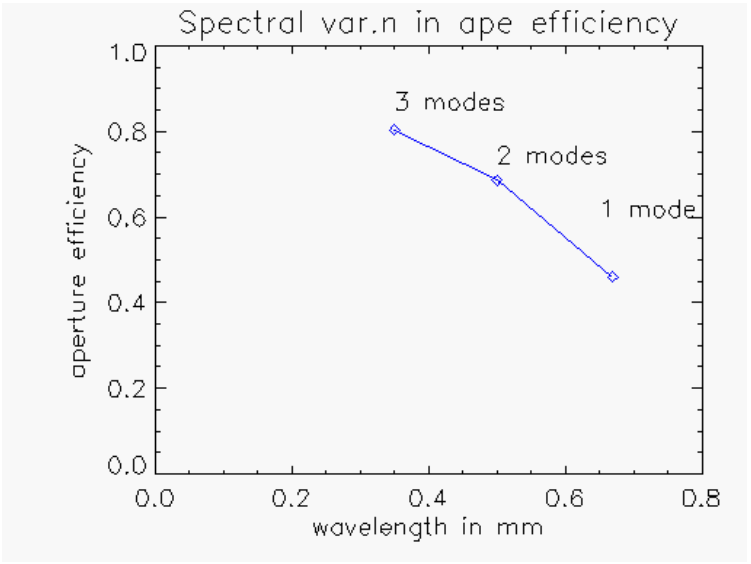

Fig.8. Aperture efficiency across the FTS longer band, for horn with λ_{des}=0.35mm.

The efficiency of the fundamental TE11 mode peaks at 0.35mm, which is expected since this is the horn design wavelength. The drop in single-mode efficiency at shorter wavelength is partly compensated for by the fact that more modes are starting to propagate.

3.2. FOV width.

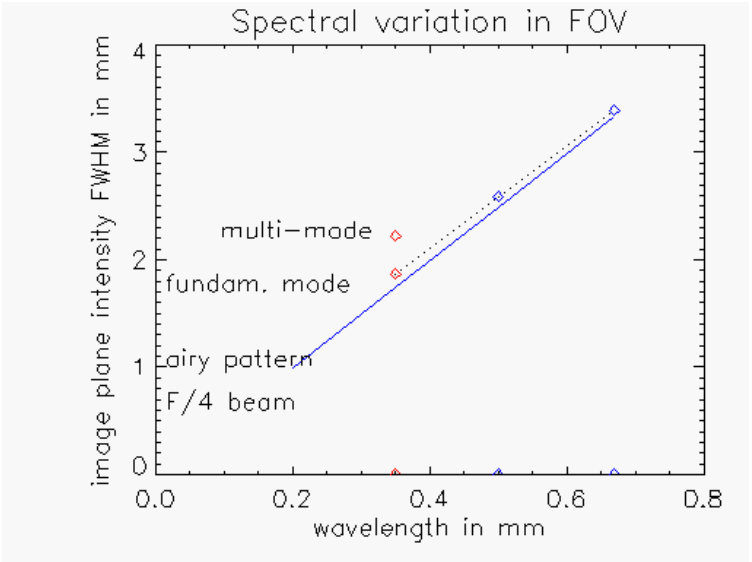

Fig.9. FOV width (in terms of averaged FWHM) across the longer FTS band.

Here we plot the 'FOV width' in terms of full-width-at-half-maximum FWHM of the antenna pattern. The asymmetry in the mode shape is not shown since we plot only the average width of the beam profiles taken in the X & Y directions of the FTS model. For comparison the width expected for a 'top-hat' beam (airy function FOV) for the F/5 pupil size is included.

a**) Single mode data.**
At the design wavelength the average FOV width of the lowest order (TE11) mode is about 10 % larger than the airy function width, and this is due to the 'underfilling' of the pupil by this gaussian-like mode shape (fig.4). This beam is clipped at approx. the 1/e amplitude level by the cold stop.

As we move to shorter wavelength the FOV width decreases only slightly, and this is due to the feature that the mode pattern at the horn is independent of wavelength. At shorter wavelength the beam at the horn aperture is larger in terms of wavelength , and this results in it filling the pupil less fully, i.e. we have '*underfilling*' and the pupil clipping or edge taper is less. At very short wavelength the FOV width would be independent of wavelength & become simply the geometric image the horn aperture mode pattern.

Moving to longer wavelengths, we have the reverse effect whereby the beam begins to *overfill* the F/5 pupil. The clipping is then more severe and the clipped TE11 beam tends to a 'top-hat'-like shape, such that the FOV width tends towards that of the airy pattern (and so starts to increases in proportion to wavelength).

b**) Multi-mode data.**
At the 0.35mm wavelength the 2 higher order modes which propagate lead to an approx. 20% increase in FOV width in terms of FWHM, but also to a change in FOV shape, as fig.10. shows.

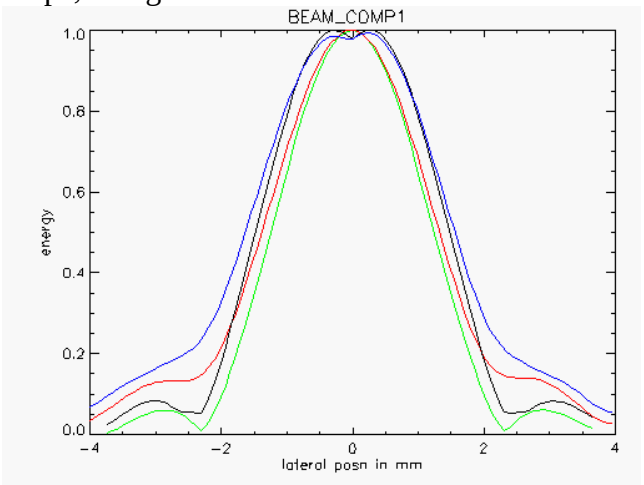

Fig.10. Net intensity beam patterns (at plane of SPIRE pick-off mirror) in single- & multi-moded cases.
Single-moded: Green= x-direction, red= y-direction.
Multi-moded : Black= x-direction, blue= y-direction.

Likewise at 0.2mm wavelength, due to the six additional modes the FOV width increase is by approx. 1/3, and the FOV shape now has minimum at its centre:

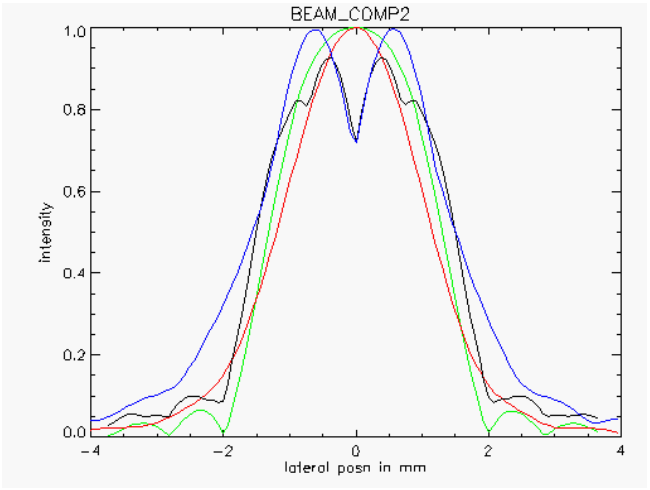

Fig.11. Net intensity beam patterns (at plane of SPIRE pick-off mirror) in single- & multi-moded cases.
Single-moded: Green= x-direction, red= y-direction.
Multi-moded : Black= x-direction, blue= y-direction.

In view of this more complicated beam pattern at short wavelength, it is also be useful to look at the corresponding pupil-plane beam patterns, and these are shown in fig.12.

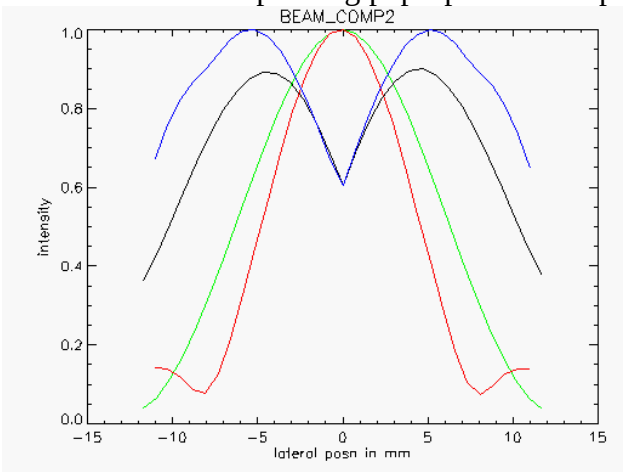

Fig.12. Net intensity beam patterns (at plane of SPIRE FTS cold stop) in single- & multi-moded cases.
Single-moded: Green= x-direction, red= y-direction.
Multi-moded : Black= x-direction, blue= y-direction.

Here it can be seen that the multi-mode aspect leads to a greater ‘filling’ of the pupil by the beam, and this should ultimately lead to the top-hat function net response expected in the limit of short wavelength (i.e. many modes propagating).

In addition there is significant asymmetry in the beam, and this is not fully shown in the above profiles. The modes involved actually have up to 6-fold symmetry in their intensity patterns, rather than just 2-fold symmetry represented in the above profiles.

Appendix A. Horn aperture efficiency.

In order to consider the interference efficiency alone, the field U of each pattern is first normalised to

$$\iint \mathrm{U}^{*}(x,y).U(x,y).dxdy = 1$$

where the integral is over the beam section, and the aperture efficiency (relative amplitude of coherently detected signal) is then given by (ref.2)

$$\mathrm{C} = \left| \iint \mathrm{U}^{*}_{\mathrm{A}}(x,y).U_{S}(x,y),dxdy \right|$$

The intensity detection efficiency is $\eta = \mathrm{C}^2$. Here the subscripts A & S refer to *aperture* (horn) & *signal* (beam) fields respectively.

The horn mode field is calculated from analytic equations, and is in scalar terms to account for unpolarised input beam.

An example field amplitude & wavefront is shown in fig.A1, for the case of L=30mm, λ=0.5mm.,λ_{des}=0.5mm.

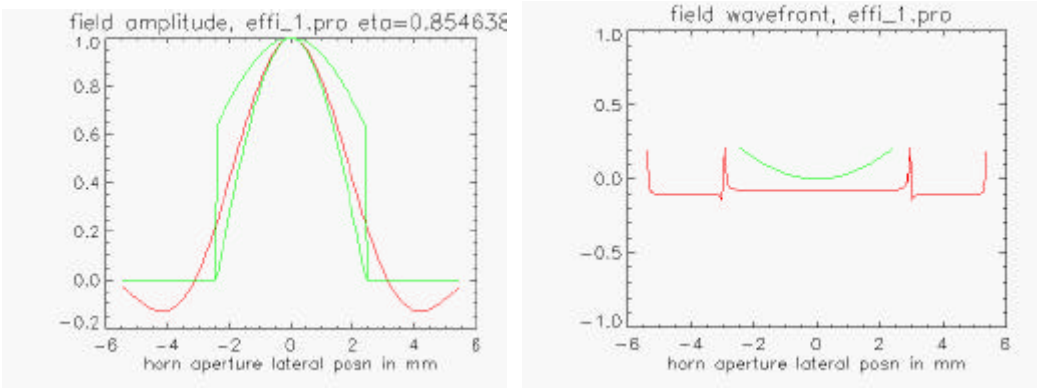

Fig.A1. Signal (red) & horn (green) field patterns at a 30mm horn at nominal focus. The signal is obtained from the ASAP propagation model of RAL note 297, and the horn is the analytic form of the smooth-wall circular horn TE11 mode. N.B. the horn amplitude pattern is not rotationally symmetric & is plotted in 2 sections (left hand graph).

In calculating the efficiency, it is necessary to use a much larger analysis window than that plotted here, in order to accurately apply the normalisations. For the case of L=30mm, the calculation gives η = 0.733. As a reference the efficiency was also calculated for the case of a x10 longer horn, L=300mm, where we find $\eta = \mathrm{C}^2$ = 0.804, quite close to the theoretical maximum of 0.814 for the case of a perfect top-

hat signal beam & 1/e clipped gaussian beam. From these results we conclude that the effect of finite horn length is to reduce the coupling by almost 7 %.

If the horn is now moved to a defocus position of –30mm, the wavefront curvature is be well-matched, as shown in fig.A2, but the amplitude pattern is then poorly fitting and the efficiency is low at η=0.605.

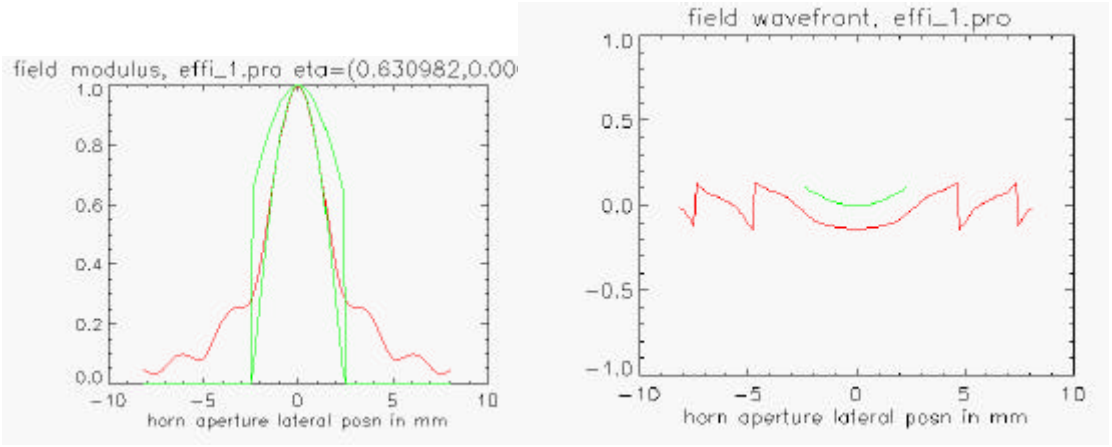

Fig.A2. Modulus & wavefront patterns as per fig.2. but with –30mm defocus applied to match wavefront curvatures (right-hand plot).

When the defocus is optimised, the result is η=0.743, at defocus of –5mm, i.e. the facility to defocus gives an improvement of 1 % in this case.

Appendix B. Conversion of mode pattern to a propagating beam. Case of TE11 mode at 0.5mm wavelength.

For propagation the field has to be converted (decomposed) into gaussian modes. Since the pattern is near a focal point and is only a few wavelengths across, this conversion is done as the angular spectrum of plane waves. For maximum resolution the angular range used is that of a full hemisphere (+- 90 degrees), for which the reconstructed pattern is as per fig.2.

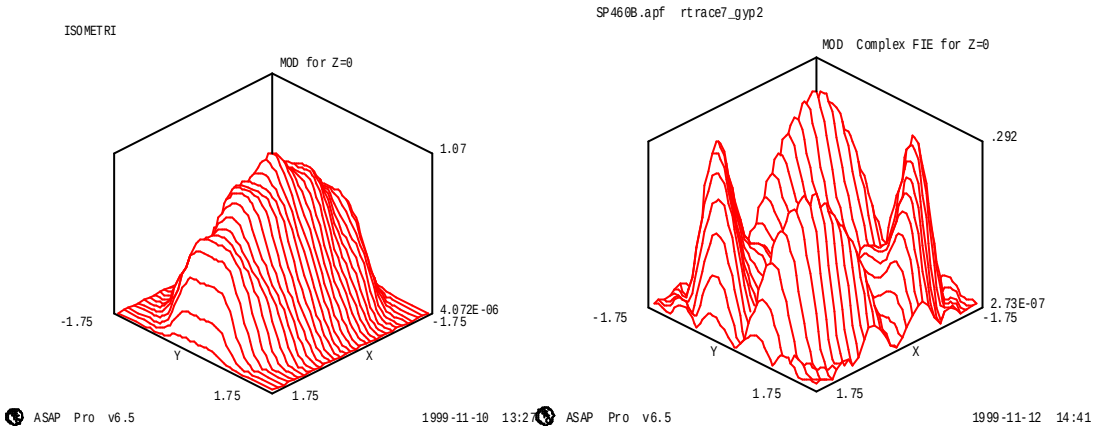

Fig.2a. Best representation in hemisphere angular spectrum ray-set (plots as per fig.1).

It is also useful to look at the total field, i.e. the resultant of the two components, as shown in fig.2b. on the right.

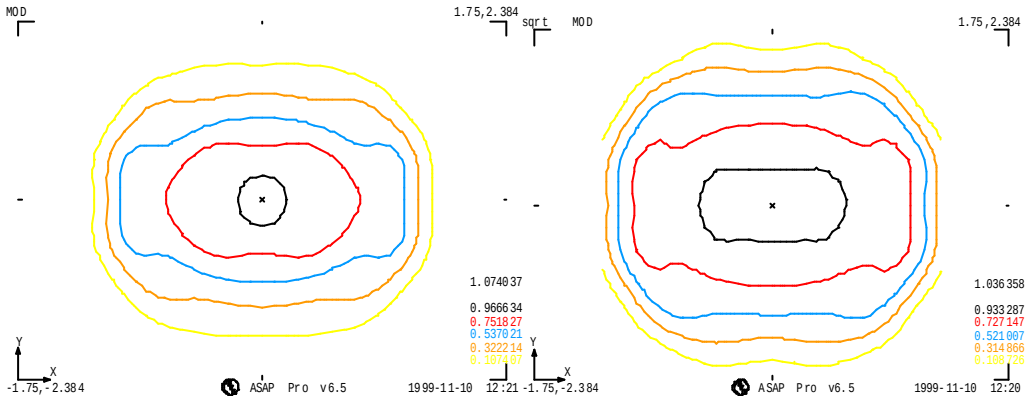

Fig.2b. Contour plot: Left: Ex component only. Right: Total field (resultant of Ex & Ey).

Comparing figures 1 & 2, there are two limitations of the accuracy of the analysis: (1) Distortion of the beam shape towards rectangular features, due to the of cartesian (x-y) sampling. (2) Limited resolution of sharp features i.e. edges. In fig.1. the sample spacing is approx. $\lambda/4$. As this is significantly less than a wavelength, some of the energy is diffracted at angles > 90 degrees, and into non-propagating evanescent modes. Also, later on the higher spatial frequencies in this pattern (angles > 10 degrees) are filtered out by the clipping action of the cold stop.

Appendix C. Beam patterns through FTS optics at longer wavelength.

1 Clipping at cold stop.

The beam is first clipped at the cold stop object #18. The beam pattern at this component is shown below.

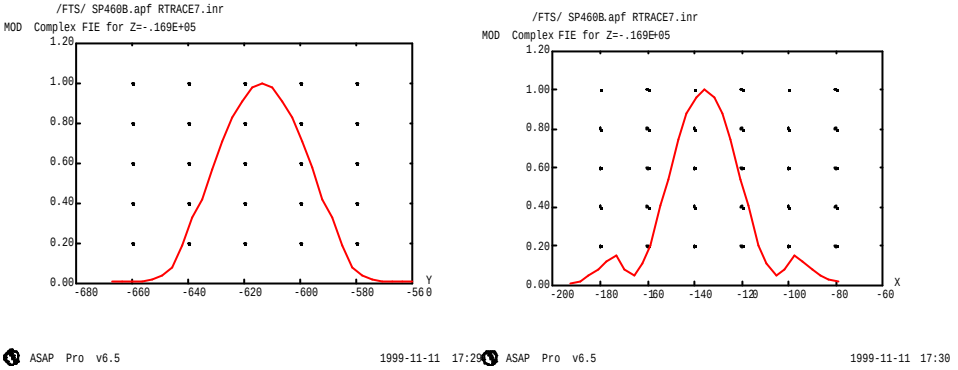

Fig.C1.a. Ex component, slices versus Y (at left) and X (right).

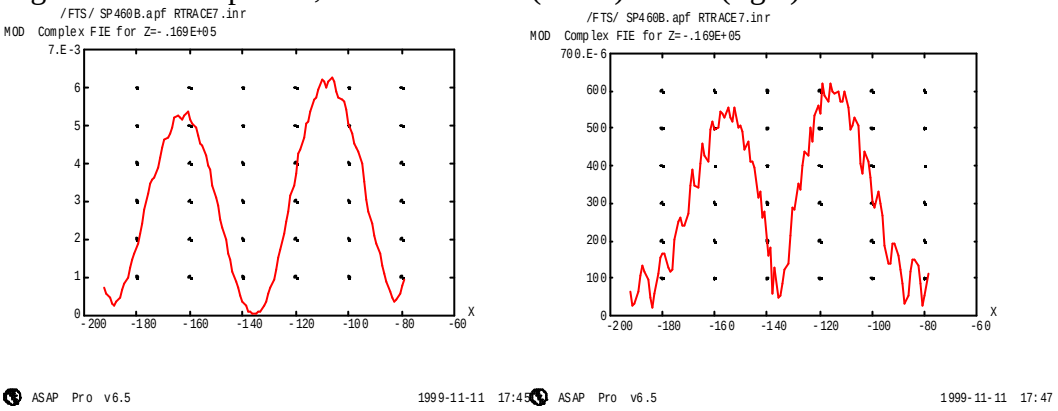

Fig.C1b. Ey component, slices in direction of maximum (45 degree from X) at left, and parallel to X (right), where magnitude is much lower.

N.B. the relative magnitudes of the peaks in Ex & Ey are Ex = 0.07, Ey=0.006.
The cold stop aperture has diameter=22.6 mm (=45 wavelengths), so only a small portion at the centre of the beam is transmitted, as shown in the figure below. For Ey this has negligible flux (the 2 sidelobes are largely blocked) & so the Ey component is not propagated further in this case.

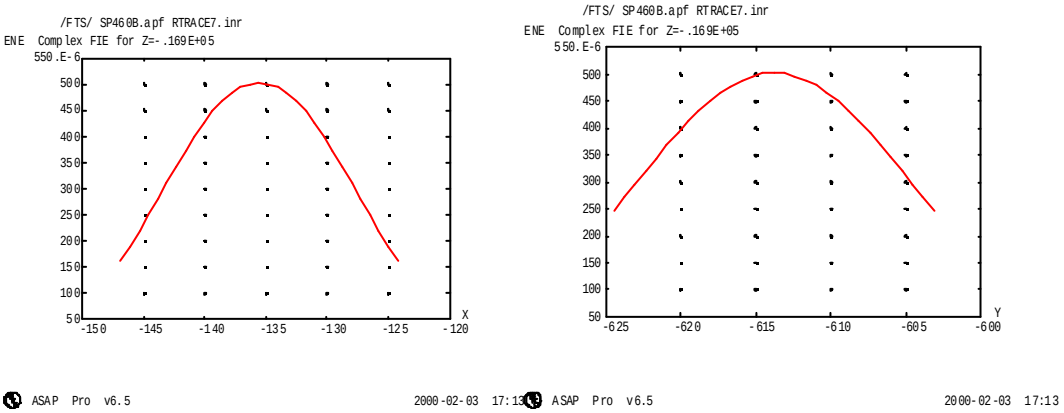

Fig.C2. ‘Ex’ plots as per fig.5a, in Energy (intensity) & with cold-stop clipping applied.

This severe clipping by the cold stop leads to the low coupling efficiency of the mode to the energy collected by the telescope at this 0.5mm wavelength, and is a consequence of the detector horn (aperture size) being designed for the shorter wavelength (0.35mm), and so it is too small to work efficiently at the longer wavelength. It is worth noting that to maximise the gain for given horn length (L=30mm here), the diameter should be approx. $\sqrt{3\lambda L}$ = 6.7mm (ref.1), approx. twice the size which is used here.

2. Rest of instrument.

The next series of plots shows the beam pattern slice versus X (i.e. perpendicular to symmetry plane) at some components of interest, in order of reverse propagation.

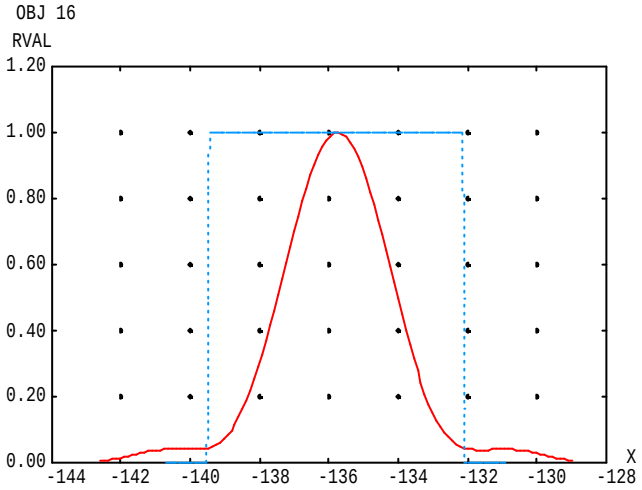

ASAP Pro v6.5 1999-11-12 13:42

Obj 16.

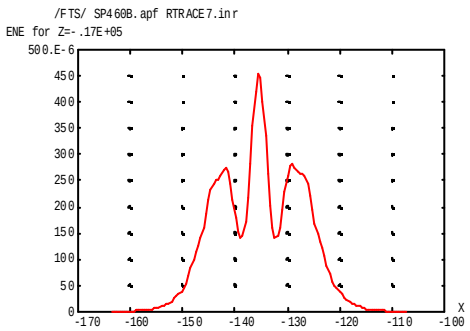

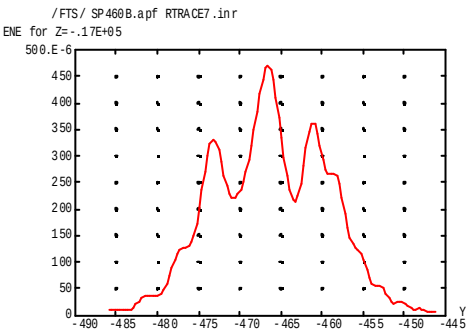

ASAP Pro v6.5 2000-02-03 17:14 ASAP Pro v6.5 2000-02-03 17:14

(a) Object 15 , interferometer collimating mirror.

N.B. the wings of the beam are significant with respect to the limited size of these collimating mirrors (diameter ~31mm). In this case the part of the beam lying on the mirror surround is not simply absorbed, since part of this surround is the adjacent collimating mirror (obj 12). However the part of the beam hitting the adjacent mirror

is reflected by it in a direction well separated from that of the signal beam, and it should be possible to trap this with a baffle between objects 12 & 11.

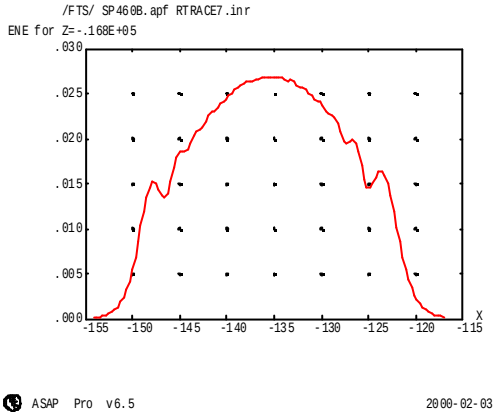

(c) Object 14, mirror face of rooftop. N.B. this is close to a pupil plane, so the beam shape regains sharper edges and similarity to that at cold stop.

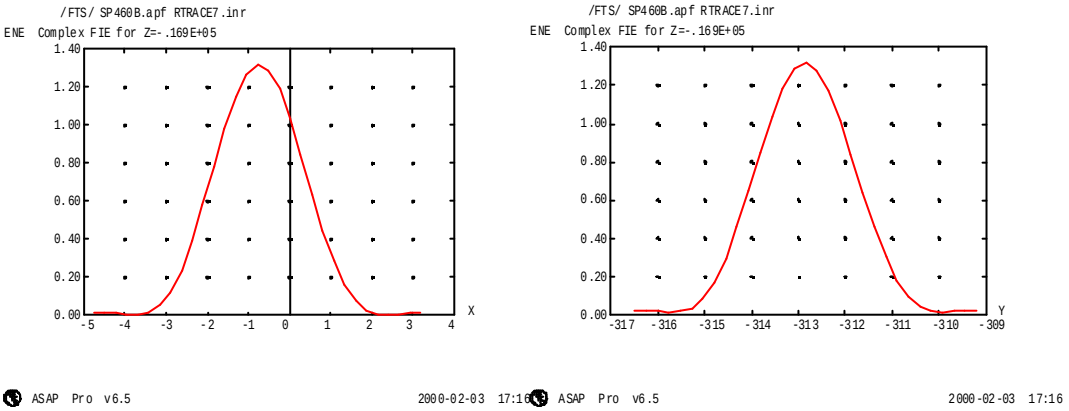

(d) Object 8, Focal plane, pick-off mirror.

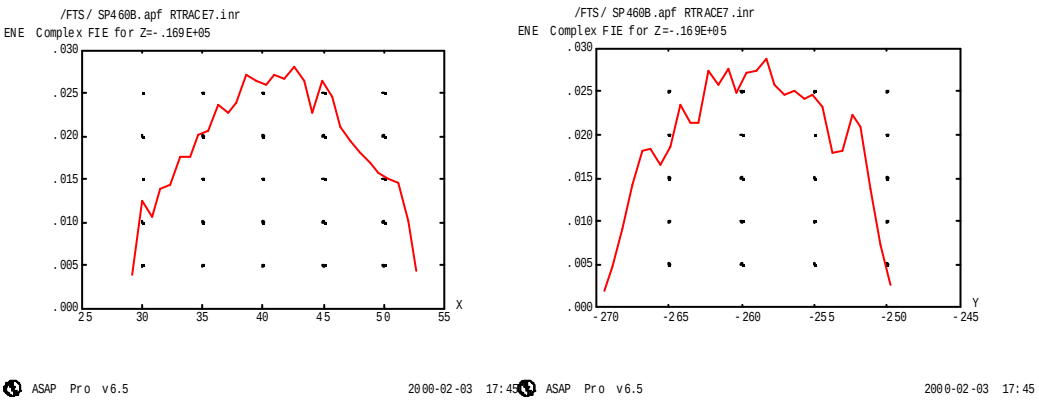

(e) Object 5. Chopper plane (pupil), in both slices.

NB the pattern here should be an image of those at the previous stops, obj 8 & 14. The noisy appearance is due to numerical errors which begin to become significant when

the set of beamlets describing the beam have been propagated through many components. The solution to this is to re-decompose the beam at some point on its way from the cold-stop to object 5.

Acknowledgement.
Thanks are due to Derek Coburn of Maynouth University for supplying the mode pattern data.

References.
Ref.1. Waveguide Handbook. Markuvitz, section 2.3.p.66.
Ref.2. MM-wave optics Lecture notes. D H Martin. Lecture 16.
Ref.3. “Aperture efficiencies of large axi-symmetric reflector antennas fed by conical horns” J.A. Murphy. IEEE Trans. AP-Vol.36, No.4 (1988)